Exchange field effects on the electronic properties of heterostructured ferromagnetic/topological crystalline insulator

B.V.Q. Ngo [a], Nguyen N. Hieu [a,b], Chu V. Lanh [c], Nguyen T.T. Anh [d], Bui D. Hoi [d,*]

[a] Institute of Research and Development, Duy Tan University, Da Nang, 550000, Viet Nam
[b] Faculty of Natural Sciences, Duy Tan University, Da Nang, 550000, Viet Nam
[c] Physics Department, Vinh Univeristy, 182 Le Duan, Vinh City, Viet Nam
[d] Department of Physics, University of Education, Hue University, 34 Le Loi, Hue City, Viet Nam

A B S T R A C T

In this paper, the exchange field effects are theoretically investigated to generate the mass in ferromagnetic/topological crystalline insulator SnTe heterostructure. The Dirac theory of exchange field-induced system predicts the *anisotropic gaps* in both low- and high-energy regimes. At small momenta, the group velocity is anisotropic, coinciding with orientation-dependent Fermi velocities, however; it increases (decreases) when the magnetization vector is parallel (antiparallel) to the host spin direction. Further, we found that the effective mass is anisotropic as well and *y*-direction is responsible for the heavy-mass band around Dirac points. Moreover, the proximity coupling leads to the switching of the effective mass sign at small momenta due to the band gap opening and concavity changing of bands. Additionally, a decreasing behavior for effective mass with exchange field strength is seen independently of the direction.

1. Introduction

Gapless phases in the band structure of novel quantum materials have attracted great interests in science and technology [1–15]. Theoretically and experimentally, such nontrivial band structures are discovered in the topological insulators (TIs), which are characterized by topological invariants [3–6,16,17]. The well-known topological invariants are the time-reversal symmetry $\mathbb{Z}_2$, chiral symmetry and the electron-hole symmetry. In such materials, topological features can be achieved from gapped bulk states and the metallic surface states [18–20]. In addition to this topological classification of band structures, crystal symmetries also lead to the topological features [18,19,21–23], which have been observed in topological crystalline insulators (TCIs).

While in strong TIs, there is an odd number of gapless surface states, in TCIs with the crystal point-group symmetries, an even number of them appears [24]. The real head of TCIs is lead thin salt family realized by angle-resolved photoemission spectroscopy (ARPES); SnTe, $Pb_{1-x}Sn_xSe$ ($x \geq 0.2$) and $Pb_{1-x}Sn_xTe$ ($x \geq 0.4$) [21–23], in which the main and important physics of them originates from the reflection symmetry [19,21–23,35]. In these TCIs, two crystal faces including metallic gapless states have been reported both theoretically and experimentally; namely (111) and {(110),(001)} surface states. The

discrepancies between the bulk Brillouin zone (BZ) and surface BZ (SBZ) in IV-VI semiconductors in reality demonstrate nice surface physics in SnTe and related alloys. For the crystal face (111), while the crystal face (001) contains four Dirac cones centered at non-time-reversal-invariant X_1 and X_2 points, four Dirac cones are centered at time-reversal-invariant Γ and M points on SBZ [19,22,23,36–38]. These SBZ points are the projected points of the bulk BZ $\{L_1, L_2, L_3, L_4\}$ points. We focus on the crystal face (001) because it shows robust surface states.

Another important difference between TCIs and TIs refers to the robustness of metallic states against the external perturbations, strong in TIs, while controllable in TCIs simply. For instance, physical external perturbations may engineer TCI phase and lead to topological phase transitions and to the reduction of spatial crystal symmetry [21,25–34]. Also, it has been found that a mechanical strain shifts the Dirac point positions and eventually leads to the band gap opening [30,31,39]. Furthermore, the time reversal symmetry breaking can happen in the presence of a magnetic dopant [40], leading to a gap opening at four Dirac points [21,41]. Additionally, applying a perpendicular electric field has introduced a topological transistors [32]. Recently, it has been reported that the electric field and staggered potential may tailor the electrical conductivity of TCI thin films [42,43]. Thus, recently, much attention has been focused on symmetry breaking in TCIs, resulting in

novel device applications.

Recent theoretical research on the valleytronics on the surface of a TCI has shown that the proximity coupling to a ferromagnet opens the gap [44]. In other words, the gaps open in the presence of the mass term originating from the exchange magnetization with an exchange field. However, the fundamental electronic properties of the system in proximity coupling a ferromagnet are left to be studied. In this paper, we investigate the proximity effects on the group velocity and effective mass of surface Dirac fermions in ferromagnetic/SnTe(001) heterostructure. Since each of the Dirac cones has a particular anisotropy, based on this, anisotropic group velocity and effective mass appear. We use the low-energy $\vec{k} \cdot \vec{p}$ model around X_1 and X_2 points in SBZ to describe the Dirac cones.

The present paper is composed as follows. In Sec. 2, the effective $\vec{k} \cdot \vec{p}$ Hamiltonian of SnTe(001) massless Dirac fermions is introduced. Also, the proximity effect is investigated on the band gap of Dirac cones in both low- and high-energy regimes. In Sec. 3, the exchange field-induced group velocity is represented. In Sec. 4, we discuss the manipulated effective mass by the proximity effect. The remarkable results are summarized in Sec. 5.

2. Theory and method

First of all, we investigate the electronic band structure of the exchange field-induced SnTe(001). The theoretical Dirac-like Hamiltonian proposed for such states including momenta $\vec{k} = (k_x, k_y)$ and the Fermi velocities $v_1 = 1.3$ eV Å and $v_2 = 2.4$ eV Å near both X_1 and X_2 points of the SBZ, respectively, is given by ($\hbar = 1$) [19,21–23,36,45]:

$$\widehat{\mathcal{H}}_{X_1}(\vec{k}) = v_1 k_x \widehat{\sigma}_y - v_2 k_y \widehat{\sigma}_x + n\widehat{\tau}_x + \delta\widehat{\sigma}_y \widehat{\tau}_y + \mathcal{M}_z \widehat{\sigma}_z, \tag{1a}$$

$$\widehat{\mathcal{H}}_{X_2}(\vec{k}) = v_2 k_x \widehat{\sigma}_y - v_1 k_y \widehat{\sigma}_x + n\widehat{\tau}_x + \delta\widehat{\sigma}_x \widehat{\tau}_y + \mathcal{M}_z \widehat{\sigma}_z, \tag{1b}$$

where $\widehat{\vec{\sigma}} = (\widehat{\sigma}_x, \widehat{\sigma}_y, \widehat{\sigma}_z)$ and $\widehat{\vec{\tau}} = (\widehat{\tau}_x, \widehat{\tau}_y)$ are the Pauli matrices in spin and sublattice [cation and anion] space, respectively. To get into the experimental observations, an intervalley scattering at the lattice scale is introduced with two parameters $n = 0.07$ eV and $\delta = 0.026$ eV [21,36]. The last term in both Hamiltonians represents the exchange magnetization with the exchange field $\mathcal{M}_z$, which arises due to proximity coupling to the ferromagnet.

These Hamiltonians are understood as follows. The transformation of $\widehat{\mathcal{H}}_{X_1}(\vec{k}) \Leftrightarrow \widehat{\mathcal{H}}_{X_2}(\vec{k})$ is valid between them because of four-fold C_4 discrete rotation symmetry described by $\widehat{\sigma}_x \mapsto \widehat{\sigma}_y$, $\widehat{\sigma}_y \mapsto -\widehat{\sigma}_x$, $k_x \mapsto k_y$, and $k_y \mapsto -k_x$. This allows us to focus on one of them, here X_1 point. To find the dispersion energy relation, we diagonalize the Hamiltonian. By this, we obtain

$$\mathcal{E}^{\mu,\nu}_{X_1}(\vec{k}) = \mu\sqrt{g(\vec{k}) + \nu h(\vec{k})}, \tag{2}$$

with

$$g(\vec{k}) = n^2 + \delta^2 + \mathcal{M}_z^2 + v_1^2 k_x^2 + v_2^2 k_y^2, \tag{3a}$$

$$h(\vec{k}) = 2\sqrt{(n^2 + \delta^2)v_1^2 k_x^2 + n^2\left(v_2^2 k_y^2 + \mathcal{M}_z^2\right)}, \tag{3b}$$

where $\mu = +1(-1)$ and $\nu = +1(-1)$ refer to the conduction (valence) band and Λ_x (Λ_x') point, respectively [see Fig. 1].

Let us assume $n = 0$, $\delta = 0$ and $\mathcal{M}_z = 0$. Immediately, one obtains

$$\mathcal{E}^{\mu}_{X_1}(\vec{k}) = \mu(v_1^2 k_x^2 + v_2^2 k_y^2)^{1/2} \text{ [if one sets } v_2 = v_1 \text{ it is similar to the}$$
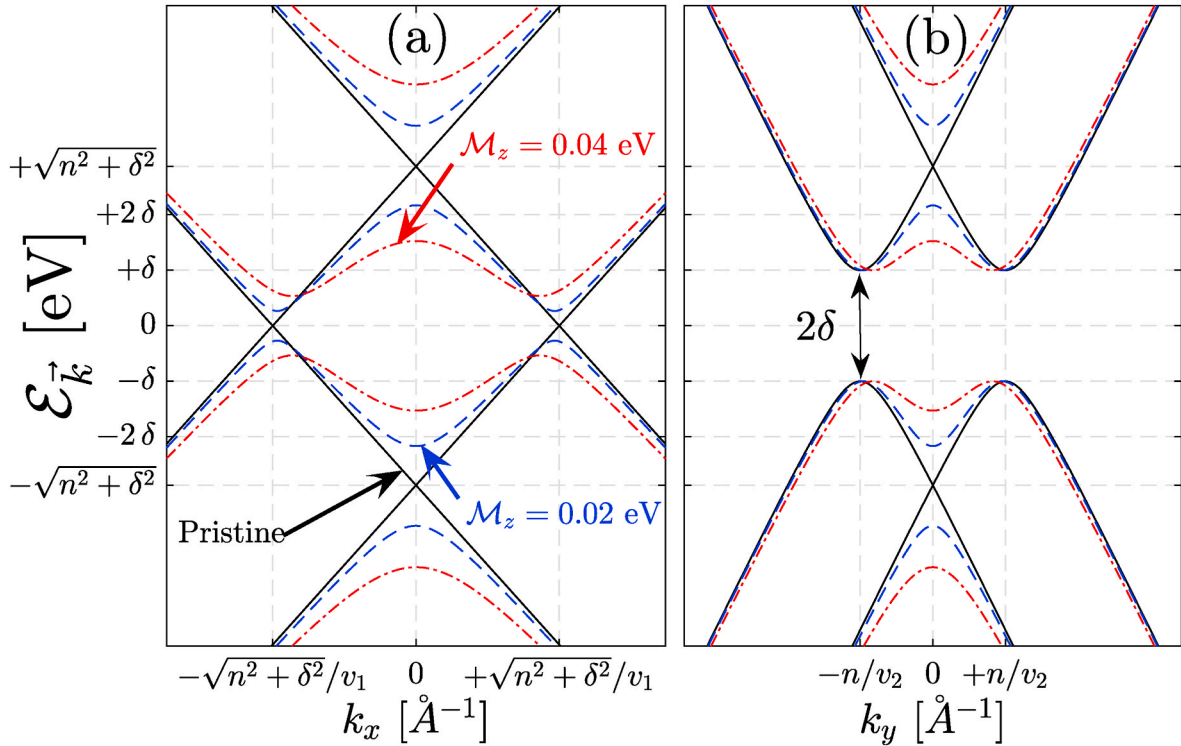

Fig. 1. Electronic band structure of Dirac fermions of the SnTe(001) in the vicinity of the X_1 point along (a) x- and (b) y-direction. Gapless and gapped phase along x- and y-direction introduce an anisotropy feature. In (a), the exchange fields with different strengths $\mathcal{M}_z = 0.02$ eV and 0.04 eV convert two massless Dirac points $\Lambda_x = (+\sqrt{n^2 + \delta^2}\,/v_1, 0)$ and $\Lambda_x' = (-\sqrt{n^2 + \delta^2}\,/v_1, 0)$ to massive ones as well as shift their position to the lower momenta. In (b), two saddle points $S_1 = (0, +n/v_2)$ and $S_2 = (0, -n/v_2)$ with energies $\pm\delta$ are shifting slightly to the lower momenta as well. Also, the gap opens at Dirac cones at $\vec{k} = 0$ with energies $\mathcal{E} = \pm\sqrt{n^2 + \delta^2}$.

graphene dispersion energy]. This, in turn, means that two copies of Dirac cones appear at the Fermi level $\mathcal{E} = 0$ and there is no separation between them. The parameter n shifts two copies of Dirac cones to cross another one. Switching on δ separates the Dirac cones, resulting in the band structure shown in Fig. 1(a). Thus, Dirac cones appear at $\Lambda_x = (+\sqrt{n^2 + \delta^2}/v_1, 0)$ and $\Lambda'_x = (-\sqrt{n^2 + \delta^2}/v_1, 0)$ points. Further, at $\vec{k} = 0$, energies $\mathcal{E} = \pm\sqrt{n^2 + \delta^2}$ appear. At $k_x = 0$, two saddle points $S_1 = (0, +n/v_2)$ and $S_2 = (0, -n/v_2)$ come up along the y direction, confirming the anisotropy property around X_1 point. These saddle points correspond to a Lifshitz transition at energies $\mathcal{E} = \pm\delta$ [21,24,25,30,31].

The electronic band structure of exchange field-induced Dirac fermions in SnTe(001) along the x- and y-direction is plotted in Fig. 1(a) and (b), respectively. When the exchange field is present, i.e. $\mathcal{M}_z = 0.02$ eV and 0.04 eV [there is no physical reason behind these values, however, we intend to set the exchange field strength comparable with and close to the intervalley scattering parameters n and δ such that our results are valid for the applied models], two new k_x points slightly away from Λ_x and Λ'_x emerge with a gap [see blue and red bands in Fig. 1(a)]. Thus, the system is not gapless in the proximity coupling to the ferromagnet and Dirac fermions on the SnTe(001) surface are massive, beneficial for the topological optoelectronics. However, since the system along the y-direction is gapped inherently with the value of 2δ, the gap size does not change significantly with $\mathcal{M}_z$, but the saddle points shift to the lower momenta. So far for the low-energy behaviors, however; for the high-energy crossed bands, a direction-independent gap opens, which increases with increasing exchange field strength. Although this figure is nice to deduce the physics of proximity coupling effects, to order its effect systematically, the energy gap of both low- and high-energy Dirac points as a function of $\mathcal{M}_z$ are plotted in the next figure.

The direction-independent band gap of high-energy Dirac points is zero for $\mathcal{M}_z = 0$ eV. This is also the case for Dirac cones at low-energy along the x-direction only, while along the y-direction, the energy gap is 2δ, as explained before. All these are confirmed in Fig. 2. Therefore, $\mathcal{E}_g^{\text{high-energy}}$ is the energy gap corresponding to the Dirac cones at $\vec{k} = 0$, while $\mathcal{E}_g^{\text{low-energy}}$ is the energy gap of Dirac cones at Λ_x and Λ'_x as well as saddle points at S_1 and S_2 points. The magnitude of the low-energy gap increases with $\mathcal{M}_z$ along the x-direction and it is symmetric concerning the sign of ferromagnet magnetization (the direction of the magnetization vector), while the gap remains unchanged along y-direction up to $\mathcal{M}_z = \pm\sqrt{n^2 + \delta^2}$. Unless noted otherwise we take -0.1 eV $\leq \mathcal{M}_z \leq +$ 0.1 eV. So, there is an anisotropy property up to this critical exchange

potential. Interestingly, the low-energy gaps become isotropic for $\mathcal{M}_z < -\sqrt{n^2 + \delta^2}$ and $\mathcal{M}_z > +\sqrt{n^2 + \delta^2}$ and both directions get the same gaps. However, this is not the case for high-energy gaps. They increase with the exchange field and are almost anisotropic for $\mathcal{M}_z \in [-0.1, +0.1]$ eV. There are two more points, where the gaps are the same. First, the point $\mathcal{M}_z \simeq \pm 3\delta/2$ in which the high-energy gap along the x-direction becomes the same as the low-energy gap along the y-direction. Second, the point $\mathcal{M}_z \simeq \pm(2\delta + \sqrt{n^2 + \delta^2})/2$ for which the low- and high-energy gaps along y-direction show the same values. These reconfirm the anisotropy feature of the system.

It should be pointed out that we restrict ourselves to the conduction bands of the band structure only in the following, since there exists electron-hole symmetry. From this point, blue and red curves in Figs. 3–6 show the lower and upper conduction band behaviors for the energy range $0 < \mathcal{E} \leq +\sqrt{n^2 + \delta^2}$ and $\mathcal{E} \geq +\sqrt{n^2 + \delta^2}$, respectively.

3. Group velocity calculations

To understand the electronic transport phenomena in TCIs in the proximity coupling to a ferromagnet, Bloch waves with wave vectors $\vec{k}$ are needed [46,47], which needs fundamental group velocity. Here, we focus on this quantity and derive its analytical expression which is strongly momentum-dependent. Ad well-known, dispersive wave packet are built from the Bloch waves, describing by the group velocity. It is generally calculated through the relation $v_\alpha^{\mu,\nu}(\vec{k}) = \partial_{k_\alpha}\mathcal{E}_{X_1}^{\mu,\nu}(\vec{k})$, where $\mu = +1$ and $\nu = +1$ (-1) refer to the conduction band and lower (upper) conduction band, respectively. Substituting Eq. (2) into $v_\alpha^{\mu,\nu}(\vec{k}) = \partial_{k_\alpha}\mathcal{E}_{X_1}^{\mu,\nu}(\vec{k})$ leads to

$$v_x^{\mu,\nu}(\vec{k}) = \frac{v_1^2 k_x}{\mathcal{E}_X^{\mu,\nu}(\vec{k})}\left(1 + 2\nu\frac{n^2 + \delta^2}{h(\vec{k})}\right), \quad v_y^{\mu,\nu}(\vec{k}) = \frac{v_2^2 k_y}{\mathcal{E}_X^{\mu,\nu}(\vec{k})}\left(1 + 2\nu\frac{n^2}{h(\vec{k})}\right) \quad (4)$$

Near and away from the Dirac points at $k_x = k_y = 0$, v_x and v_y behave differently for both lower and upper conduction bands, coinciding with the v_1 and v_2, respectively. It is clear that the intervalley scattering parameters n and δ play important roles in the real-space motion of fermions. If we assume that $n = 0$, $\delta = 0$ and $\mathcal{M}_z = 0$, we obtain $v_x^\mu(\vec{k}) = v_1^2 k_x/\mu(v_1^2 k_x^2 + v_2^2 k_y^2)^{1/2}$ and $v_y^\mu(\vec{k}) = v_2^2 k_y/\mu(v_1^2 k_x^2 + v_2^2 k_y^2)^{1/2}$. If we
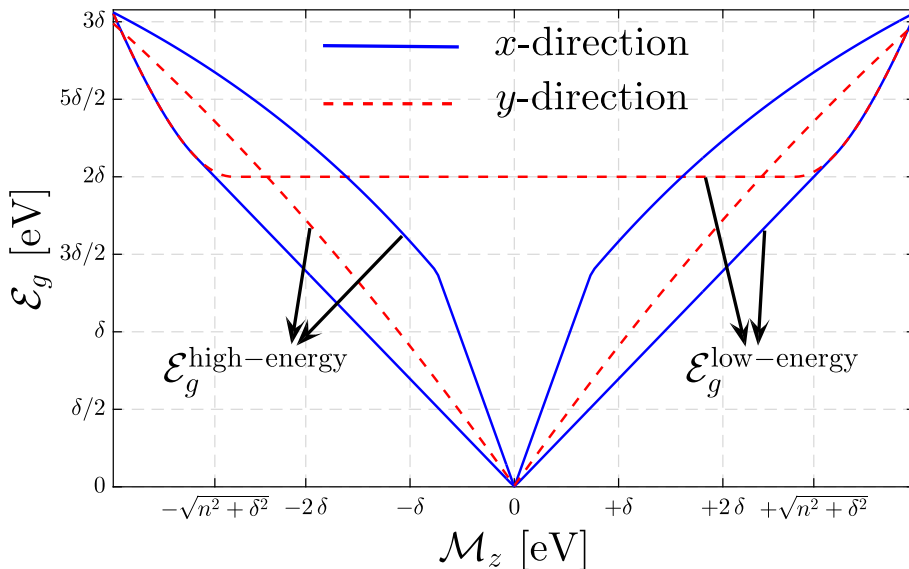

Fig. 2. Low- and high-energy gap of surface fermions in TCI SnTe(001) as a function of exchange field $\mathcal{M}_z$. The solid blue (dashed red) curve is for the x (y) direction. In the absence of $\mathcal{M}_z$, the high-energy gaps are zero in both directions, while the low-energy gap is zero and 2δ along the x- and y- direction, respectively. Both low- and high-energy gaps are modulated with the exchange field. (For interpretation of the references to colour in this figure legend, the reader is referred to the Web version of this article.)
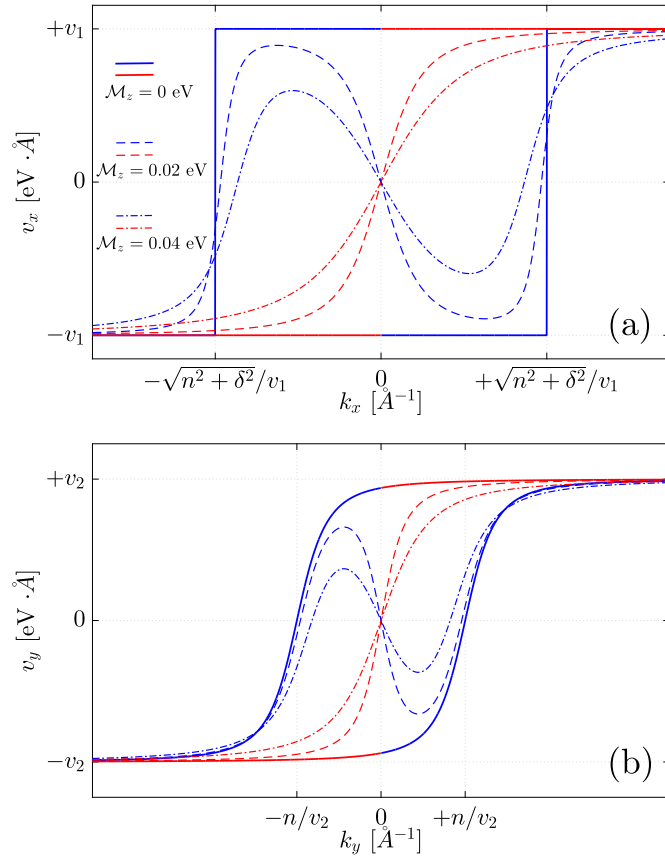
Fig. 3. The group velocity of Dirac fermions in gapless and gapped SnTe(001) TCI along the (a) *x*- and (b) *y*-direction. The Fermi velocities and critical momenta corresponding to the Dirac points and saddle points are labeled in the axes.
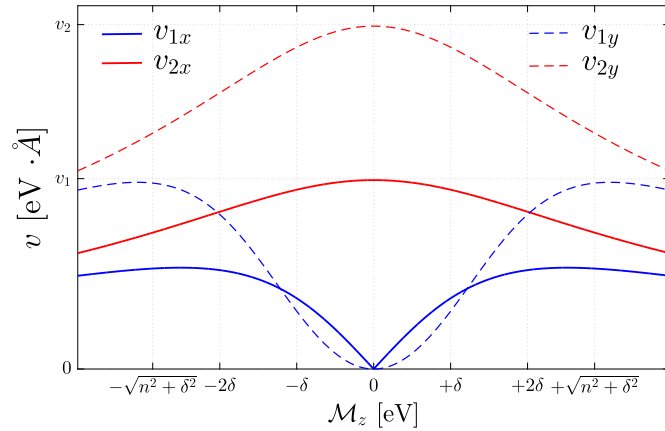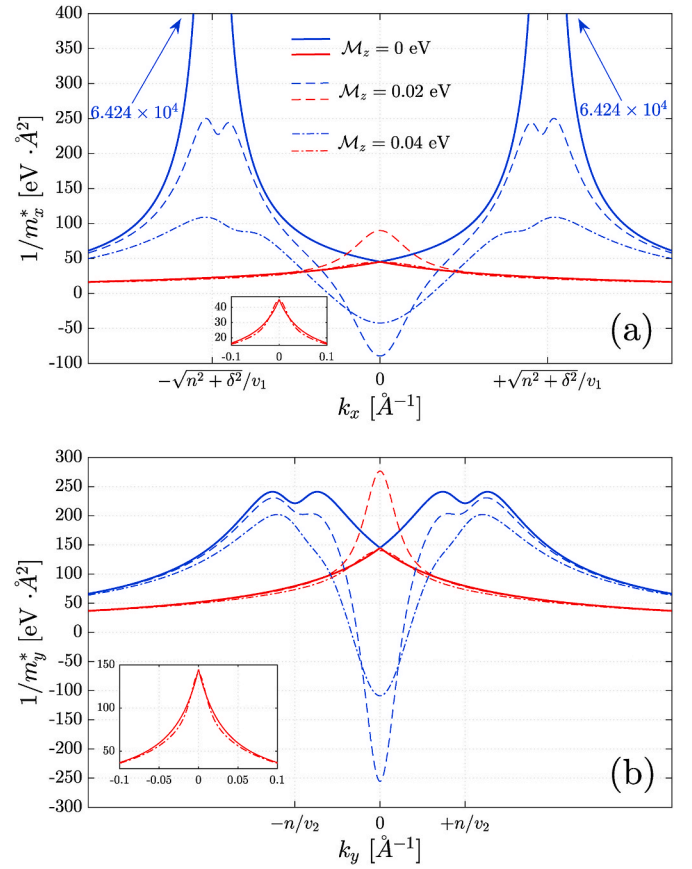

Fig. 5. Effective mass of surface massless and massive Dirac fermions in SnTe (001) TCI along the (a) *x*- and (b) *y*-direction.

Fig. 4. group velocity of surface fermions in SnTe(001) as a function of exchange field $\mathcal{M}_z$ along both the *x*- and *y*-direction. For the *x*-direction, we fix $k_y = 0$ and $k_x = +\sqrt{n^2 + \delta^2}/v_1$ and for the *y*-direction we fix $k_x = 0$ and $k_y = +n/v_2$.

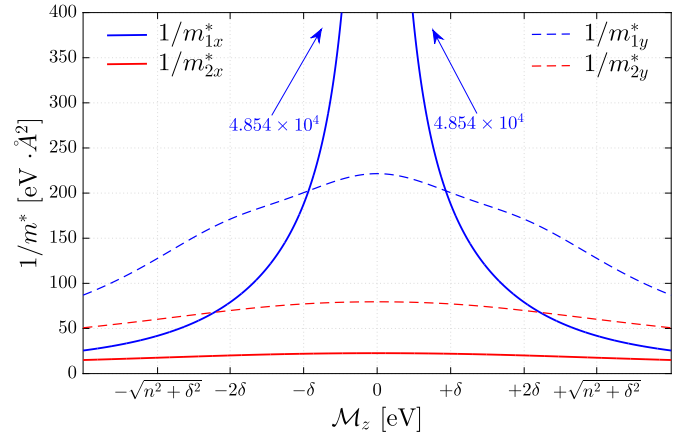**Fig. 6.** Effective mass of Dirac fermions in SnTe(001) as a function of exchange field $\mathcal{M}_z$ along both *x*- and *y*-direction. For the *x*-direction, we fix $k_y = 0$ and $k_x = +\sqrt{n^2 + \delta^2}/v_1$ and for the *y*-direction we fix $k_x = 0$ and $k_y = +n/v_2$.

switch on n and δ only, not $\mathcal{M}_z$, we have

$$
v_x^\nu(k_x) = \frac{v_1}{\mathcal{E}_X^\nu(k_x, 0)}\left(v_1 k_x + \nu\sqrt{n^2 + \delta^2}\right), \; v_y^\nu(k_y) = \frac{v_2}{\mathcal{E}_X^\nu(0, k_y)}\left(v_2 k_y + \nu n\right)
\tag{5}
$$

The direction-dependent group velocity of Dirac fermions is plotted in

Fig. 3 without and with proximity coupling. Fig. 3(a) illustrates that in the absence of exchange field, $\mathcal{M}_z = 0$ eV, the group velocity of upper conduction band [solid red curves] along the *x*-direction is $+v_1$ ($-v_1$) for the momenta $k_x \geq 0$ ($k_x \leq 0$), while the group velocity of the lower conduction band [solid blue curves] is $+v_1$ ($-v_1$) for the range of $-\sqrt{n^2 + \delta^2}/v_1 < k_x \leq 0$ ($0 \leq k_x < +\sqrt{n^2 + \delta^2}/v_1$) and at $k_x = \pm\sqrt{n^2 + \delta^2}/v_1$, it is zero. These trends can be confirmed by the slope of the bands in Fig. 1 because from zero to the Dirac points as well as after the Dirac points opposite slopes can be seen for the lower conduction

band. And opposite slopes from zero to the Dirac points and after them are evident for the upper conduction band as well. Similarly, Fig. 3(b) shows that for $\mathcal{M}_z = 0$ eV, for the momentum $k_y < -n/v_2$ and $k_y > +n/v_2$, the group velocity of Dirac fermions along the y-direction is $-v_2$ and $+v_2$, respectively for the upper conduction band (the red curves). However, it is slightly away from these Fermi velocities when the momentum takes the value in the range of $-n/v_2 \leq k_y \leq 0$ and $0 \leq k_y \leq +n/v_2$, due to the parabolic bands at saddle points. It is expected from Fig. 1 that v_y for the lower conduction band is zero at saddle points $k_y = \pm n/v_2$ [see blue curves]. Interestingly, the curves approach the Fermi velocities $\pm v_2$ before and after these saddle points. So, no significant change can be observed in the group velocity of upper conduction band, implying that at $k_x = 0$ Dirac fermions have the same velocities, independent of the k_y momentum, while the lower band of the conduction band (blue band) changes significantly with $\pm k_y$.

Let us turn to the presence of the exchange field $\mathcal{M}_z$. For non-zero exchange fields, we again have Eq. (4) for group velocity along the x- and y-direction, respectively. Two exchange fields 0.02 eV and 0.04 eV are examined to understand the proximity coupling effects on v_x and v_y. We see that the directions of the velocities are not identical if the sign of momenta switches as well as the continuous group velocities come up in contrast to the discrete group velocities in the pristine case. In Fig. 3(a), the velocities for the lower conduction band are not zero at Dirac points for $\mathcal{M}_z \neq 0$ because of the band gap opening in the band structure, which leads to the extrema with $v_x \neq \pm v_1$. For the upper conduction band, the same behaviors appear without extrema. However, the group velocity of conduction bands converges to the $\pm v_1$ at high momenta, in agreement with Fig. 1. As for the y-direction, the group velocity versus k_y indicates the same curves, as illustrated in Fig. 3(b). There are still two extrema k_y-points for the lower conduction band, but in different coordinates, for which the group velocity is close to $\pm v_2$. Also, v_y is not zero at saddle points due to the shifted k_y [see Fig. 1]. As expected, the upper conduction band should behave as the x-direction because of the same opening band gap trends discussed before.

It is a fact that the magnitudes of the group velocity of conduction bands depend on the exchange field strength. Let us to systematically study v_{1x}, v_{2x}, v_{1y}, and v_{2y}, respectively, corresponding to the lower conduction band, upper conduction band along the x-direction, lower conduction band, and upper conduction band along the y-direction as a function of $\mathcal{M}_z$. To do so, $k_y = 0$ and $k_x = +\sqrt{n^2 + \delta^2}/v_1$ as well as $k_x = 0$ and $k_y = +n/v_2$ are considered along the x- and y-direction, respectively. We illustrate them in Fig. 4. The group velocities are found to exhibit opposite behaviors when the magnetization vector of the ferromagnet is parallel or antiparallel to the host spin directions, which corresponds to the sign of $\mathcal{M}_z$; $+$ for parallel magnetization and $-$ for antiparallel one. In the absence of proximity coupling, $\mathcal{M}_z = 0$, as expected from Fig. 3, both v_{1x} and v_{1y} are zero while $v_{2x} = +v_1$ and $v_{2y} = +v_2$. Once the proximity coupling is considered, $\{v_{1x}, v_{1y}\}$ ($\{v_{2x}, v_{2y}\}$) increase (decrease) with $\mathcal{M}_z > 0$ ($\mathcal{M}_z < 0$). However, it is necessary to report that after the critical exchange fields $\pm\sqrt{n^2 + \delta^2}$, the group velocity of lower conduction bands along both directions starts to decrease slightly.

4. Effective mass calculations

It is the time to study the concept of effective mass, which has many different definitions [48–51]. In a nutshell, to understand the fundamental electro-optical properties of a system, effective mass comes into play role. However, to design and develop the heterostructured ferromagnet/SnTe(001), the synergy of effective mass in quantum transport of the system is needed to be investigated and has not been reported to date. It is common to use the second derivative of $\mathcal{E}_{X_1}^{\mu,\nu}(\vec{k})$ along the $\alpha \in \{x, y\}$ direction, $1/m_\alpha^{*\mu,\nu}(\vec{k}) = \partial_{k_\alpha}^2 \mathcal{E}_{X_1}^{\mu,\nu}(\vec{k})$. Substituting Eq. (2) into the above equation leads to the following expression along the x-direction

$$\frac{1}{m_x^{*\mu,\nu}(\vec{k})} = -\frac{v_1^4 k_x^2}{\left[\mathcal{E}_X^{\mu,\nu}(\vec{k})\right]^3}\left(1 - 2\nu\frac{n^2 + \delta^2}{h(\vec{k})}\right)^2 - \frac{v_1^2}{\mathcal{E}_X^{\mu,\nu}(\vec{k})}\left(1 + 8\nu\frac{v_1^2 k_x^2(n^2 + \delta^2)^2}{h^3(\vec{k})}\right.$$
$$\left. - 2\nu\frac{n^2 + \delta^2}{h(\vec{k})}\right),$$

(6)

as well as along the y-direction, we obtain

$$\frac{1}{m_y^{*\mu,\nu}(\vec{k})} =$$
$$-\frac{v_2^4 k_y^2}{\left[\mathcal{E}_X^{\mu,\nu}(\vec{k})\right]^3}\left(1 - 2\nu\frac{n^2}{h(\vec{k})}\right)^2$$
$$-\frac{v_2^2}{\mathcal{E}_X^{\mu,\nu}(\vec{k})}\left(1 + 8\nu\frac{v_2^2 k_y^2 n^4}{h^3(\vec{k})} - 2\nu\frac{n^2}{h(\vec{k})}\right)$$

(7)

Since the electron-hole symmetry is present, similar to the group velocity case, herein we focus on the conduction bands only. Again, $1/m_x^*$ and $1/m_y^*$ are anisotropic and the intervalley scattering parameters n and δ play key roles in the effective mass of fermions. If we assume that $n = 0$, $\delta = 0$ and $\mathcal{M}_z = 0$, we obtain $1/m_x^{*\mu}(\vec{k}) = -(v_1^2/\mathcal{E}_X^\mu(\vec{k}))[1 + (v_1^2 k_x^2/\mathcal{E}_X^{2,\mu}(\vec{k}))]$ and $1/m_y^{*\mu}(\vec{k}) = -(v_2^2/\mathcal{E}_X^\mu(\vec{k}))[1 + (v_2^2 k_y^2/\mathcal{E}_X^{2,\mu}(\vec{k}))]$.

Let us explain the physical meaning of the effective mass. Theoretically, the concavity up and down of bands can be understood from the sign of effective mass. On the one hand, the concavity of energy bands in the band structure determines the degeneracy of them in the density of states diagram. On the other hand, the concavity of a band demonstrates the EM of fermions in the band with a special wave-vector. As can be seen in Fig. 1, one finds $m_x^* < m_y^*$ [the heavy (light)-mass along the y (x)-direction] for the lower conduction bands should be valid independent of the momenta or exchange field $\mathcal{M}_z$, implying that the energy separation between band edges along the y-direction is considerably greater than the x-direction.

The results are plotted in Fig. 5(a) and (b) for two typical wave-vectors $k_y = 0$ and $k_x = 0$. Let us assume that $\mathcal{M}_z = 0$ eV. In this case, Eq. (6) gives rise to two singularities at Dirac points as well as Eq. (7) shows two humps at saddle points. Similar to the group velocity, for $k_x = k_y = 0$ values, the effective mass of both conduction bands along each direction is isotropic, while for non-zero momenta, $1/m_x^*$ of the lower conduction band [solid blue curve] increases up to $k_x = |\sqrt{n^2 + \delta^2}|$ and decreases after that. However, $1/m_x^*$ of the upper conduction band [solid red curve] decreases with k_x [see Fig. 5(a)]. The maximum value of effective mass takes place at $k_x = \pm\sqrt{n^2 + \delta^2}/v_1$ along the x-direction for the lower conduction band, whilst it is (on average) the case at $k_y = \pm n/v_2$ for effective mass along the y-direction.

Let us focus on the exchange field-induced effective mass of surface Dirac fermions in SnTe(001). We analyze the particular cases of exchange fields 0.02 eV and 0.04 eV along both x- and y-direction, as shown in Fig. 5(a) and (b). It can be observed from Fig. 5(a) that when $\mathcal{M}_z$ appears, the positive $1/m_x^*$ of the lower conduction band decreases with exchange field at Dirac points with a factor of 250 due to the band gap opening and becomes negative at $k_x = \pm\sqrt{n^2 + \delta^2}/4v_1$ and $k_x = \pm 3\sqrt{n^2 + \delta^2}/8v_1$ for $\mathcal{M}_z = 0.02$ eV and 0.04 eV, respectively. This can be understood from the concavity of curves at small momenta in the band structure easily. Such effective mass sign switching does not occur for the upper conduction band [see red curves] and the effective mass is positive for both exchange fields. However, in contrast to the lower conduction band, $1/m_x^*$ of the upper conduction band increases first with a factor of 2 and then comes back to close to the initial concavity when

$\mathcal{M}_z$ becomes stronger [see the inset panel in Fig. 5(a)].

For the Fig. 5(b), which describes the $1/m_y^*$ versus k_y at $k_x = 0$, the effects caused by the proximity coupling in the effective mass are different than the one along the x-direction because of the inherent anisotropy feature in SnTe(001) Dirac cones. The trend is decreasing for lower conduction band with a factor of 0.5 and again the effective mass sign changes with exchange field 0.02 eV and 0.04 eV at $k_y = \pm n/4v_2$ and $k_y = \pm 3n/8v_2$, respectively. Interestingly, the effective mass of the upper conduction band does not show any sign switching with the exchange field $\mathcal{M}_z$ and increases with the exchange field first with a factor of 2 and gets the initial value as the proximity coupling is increased. The changes are for the small momenta and for large momenta, the effective masses behave similarly independent of the exchange field strength.

The systematic study of $1/m_{1x}^*$, $1/m_{2x}^*$, $1/m_{1y}^*$, and $1/m_{2y}^*$ corresponding to the lower conduction band, upper conduction band along the x-direction, lower conduction band, and upper conduction band along the y-direction, respectively, as a function of $\mathcal{M}_z$ is plotted in Fig. 6. It is clear from Fig. 6 that m_{1x}^* has the minimum value (because $1/m_{1x}^*$ has the maximum value) at $k_y = 0$ and $k_x = +\sqrt{n^2 + \delta^2}/v_1$ and decreases with $|\mathcal{M}_z|$, while m_{2x}^* possesses the maximum value (because $1/m_{2x}^*$ has the minimum value) and it is almost constant and independent of the exchange field strength. The most dramatic sign of the upper conduction band is that the behavior near the neutrality point changes with a few orders of magnitude difference when the ferromagnet is in the proximity with SnTe(001) surface. This is the same for the y-direction, meaning that both conduction bands along the y-direction decrease with the exchange field with a symmetry property.

5. Summary

In summary, the proximity effects in a ferromagnet/SnTe(001) heterostructure on the surface Dirac fermions protected by the mirror symmetry have been investigated. The surface allows the use of $\vec{k}\cdot\vec{p}$ theory and traditional semi-classical approach. We have obtained the exchange field-dependence of the band gap, group velocity and effective mass. In their evaluation, we have incorporated effects from momentum and intervalley scattering processes. Our findings indicated that the electronic properties including the electronic band structure, group velocity and effective mass are anisotropic. We found that while the induced exchange field does suppress the TCI phase, the band gap opens. In addition, we found that while the exchange field-induced group velocity and effective mass may be enhanced near the Dirac points and saddle points along the x- and y-direction, respectively, they can be tuned through the magnetization direction and module with the symmetry feature. Our work reveals an interesting link between proximity effect and topological features to heterostructures based on TCI and may find applications in topological optoelectronics.

Author contributions

B. V. Q. Ngo: Conceptualization, Investigation, Formal analysis, Revising, Writing and Editing. **Nguyen N. Hieu**: Conceptualization, Investigation, Formal analysis, Revising, Writing and Editing. **Chu V. Lanh**: Software, Formal analysis, Writing – Review and Editing. **Nguyen T. T. Anh**: Conceptualization, Investigation, Software, Formal analysis. **Bui D. Hoi**: Conceptualization, Methodology, Investigation, Formal analysis, Writing – Review and Editing.

Declaration of competing interest

The authors declare that they have no known competing financial interests or personal relationships that could have appeared to influence the work reported in this paper.

References

[1] B.A. Bernevig, T.L. Hughes, S.-C. Zhang, Science 314 (2006) 1757.
[2] M. König, S. Wiedmann, C. Brüne, A. Roth, H. Buhmann, L.W. Molenkamp, X.-L. Qi, S.-C. Zhang, Science 318 (2007) 766.
[3] M.Z. Hasan, C.L. Kane, Rev. Mod. Phys. 82 (2010) 3045.
[4] X.-L. Qi, S.-C. Zhang, Rev. Mod. Phys. 83 (2011) 1057.
[5] A. Bansil, H. Lin, T. Das, Rev. Mod. Phys. 88 (2016), 021004.
[6] L. Fu, C.L. Kane, E.J. Mele, Phys. Rev. Lett. 98 (2007), 106803.
[7] D.J. Thouless, M. Kohmoto, M.P. Nightingale, M. den Nijs, Phys. Rev. Lett. 49 (1982) 405.
[8] S.-Y. Xu, Y. Xia, L.A. Wray, S. Jia, F. Meier, J.H. Dil, J. Osterwalder, B. Slomski, A. Bansil, H. Lin, R.J. Cava, M.Z. Hasan, Science 332 (2011) 560.
[9] M. Yarmohammadi, Phys. Lett. A 381 (14) (2017) 1261.
[10] M. Brahlek, N. Bansal, N. Koirala, S.-Y. Xu, M. Neupane, C. Liu, M.Z. Hasan, S. Oh, Phys. Rev. Lett. 109 (2012), 186403.
[11] S.-Y. Xu, C. Liu, N. Alidoust, M. Neupane, D. Qian, I. Belopolski, J.D. Denlinger, Y. J. Wang, H. Lin, L.A. Wray, G. Landolt, B. Slomski, J.H. Dil, A. Marcinkova, E. Morosan, Q. Gibson, R. Sankar, F.C. Chou, R.J. Cava, A. Bansil, M.Z. Hasan, Nat. Commun. 3 (2012) 2191.
[12] M. Yarmohammadi, RSC Adv. 7 (18) (2017) 10650.
[13] J. Zhang, W.-X. Ji, C.-W. Zhang, P. Li, P.-J. Wang, Phys. Chem. Chem. Phys. 20 (2018) 24790.
[14] R.-W. Zhang, C.-W. Zhang, W.-X. Ji, S.-S. Li, S.-J. Hu, S.-S. Yan, P. Li, P.-J. Wang, F. Li, New J. Phys. 17 (2015), 083036.
[15] P.T.T. Le, T.C. Phong, M. Yarmohammadi, Phys. Chem. Chem. Phys. 21 (2019) 21790.
[16] A.P. Schnyder, S. Ryu, A. Furusaki, A.W.W. Ludwig, Phys. Rev. B 78 (2008), 195125.
[17] A. Kitaev, AIP Conf. Proc. 1134 (2009) 22.
[18] L. Fu, Phys. Rev. Lett. 106 (2011), 106802.
[19] S.-Y. Xu, C. Liu, N. Alidoust, M. Neupane, D. Qian, I. Belopolski, J. Denlinger, Y. Wang, H. Lin, L. Wray, G. Landolt, B. Slomski, J. Dil, A. Marcinkova, E. Morosan, Q. Gibson, R. Sankar, F. Chou, R. Cava, A. Bansil, M. Hasan, Nat. Commun. 3 (2012) 1192.
[20] R.S.K. Mong, A.M. Essin, J.E. Moore, Phys. Rev. B 81 (2010), 245209.
[21] T.H. Hsieh, H. Lin, J. Liu, W. Duan, A. Bansil, L. Fu, Nat. Commun. 3 (2012) 982.
[22] P. Dziawa, B.J. Kowalski, K. Dybko, R. Buczko, A. Szczerbakow, M. Szot, E. Łusakowska, T. Balasubramanian, B.M. Wojek, M.H. Berntsen, O. Tjernberg, T. Story, Nat. Mater. 11 (2012) 1023.
[23] Y. Tanaka, Z. Ren, T. Sato, K. Nakayama, S. Souma, T. Takahashi, K. Segawa, Y. Ando, Nat. Phys. 8 (2012) 800.
[24] Y. Ando, L. Fu, Annu. Rev. Condens. Matter Phys. 6 (2015) 361.
[25] M. Yarmohammadi, K. Mirabbaszadeh, Phys. Chem. Chem. Phys. 21 (2019) 21633.
[26] M. Yarmohammadi, K. Mirabbaszadeh, J. Mater. Chem. A 7 (2019) 25573.
[27] P. Barone, D. Di Sante, S. Picozzi, Phys. Status Solidi RRL 7 (2013) 1102.
[28] L. Zhao, J. Wang, B.-L. Gu, W. Duan, Phys. Rev. B 91 (2015), 195320.
[29] Y. Tanaka, T. Sato, K. Nakayama, S. Souma, T. Takahashi, et al., Phys. Rev. B 87 (2015), 155105.
[30] M. Serbyn, L. Fu, Phys. Rev. B 90 (2014), 035402.
[31] E. Tang, L. Fu, Nat. Phys. 10 (2014) 964.
[32] J. Liu, T.H. Hsieh, P. Wei, W. Duan, J. Moodera, et al., Nat. Mater. 13 (2014) 178.
[33] X. Qian, L. Fu, J. Li, Nano Res. 8 (2015) 967.
[34] L. Fu, C.L. Kane, Phys. Rev. Lett. 109 (2012), 246605.
[35] J.C.Y. Teo, L. Fu, C.L. Kane, Phys. Rev. B 78 (2008), 045426.
[36] J. Liu, W. Duan, L. Fu, Phys. Rev. B 88 (2013), 241303(R).
[37] Y. Tanaka, T. Shoman, K. Nakayama, S. Souma, T. Sato, T. Takahashi, M. Novak, K. Segawa, Y. Ando, Phys. Rev. B 88 (2013), 235126.
[38] C.M. Polley, P. Dziawa, A. Reszka, A. Szczerbakow, R. Minikayev, J.Z. Domagala, S. Safaei, P. Kacman, R. Buczko, J. Adell, M.H. Berntsen, B.M. Wojek, O. Tjernberg, B.J. Kowalski, T. Story, T. Balasubramanian, Phys. Rev. B 89 (2014), 075317.
[39] O.I. Yuzephovich, M.Y. Mikhailov, S.V. Bengus, A.Y. Aladyshkin, E.E. Pestov, et al., Low Temp. Phys. 34 (2008) 985.
[40] P. Sessi, D. Di Sante, A. Szczerbakow, F. Glott, S. Wilfert, H. Schmidt, T. Bathon, P. Dziawa, M. Greiter, T. Neupert, G. Sangiovanni, T. Story, R. Thomale, M. Bode, Science 354 (2016) 1269.
[41] C. Fang, M.J. Gilbert, B.A. Bernevig, Phys. Rev. Lett. 112 (2012), 046801.
[42] H.D. Bui, M. Yarmohammadi, Phys. E Low-dimens. Syst. Nanostruct. 124 (2020), 114330.
[43] V.C. Nguyen, B.D. Hoi, M. Yarmohammadi, J. Phys. D Appl. Phys. 53 (2020), 425301.
[44] M. Ezawa, Phys. Rev. B 89 (2014), 195413.
[45] Y. Okada, M. Serbyn, H. Lin, D. Walkup, W. Zhou, et al., Science 341 (2013) 1496.
[46] G.D. Mahan, Many Particle Physics, Plenum Press, New York, 1993.
[47] G. Grosso, G.P. Parravicini, Solid State Physics, Academic Press, New York, 2014.
[48] N.W. Aschcroft, Solid State Theory, Holt, Rinehart, and Wilson, 1976.
[49] K. Seeger, Semiconductor Physics, Springer-Verlag, 1985.
[50] W.A. Harrison, Solid State Theory, Dover, 1979.
[51] D. Walkup, B.A. Assaf, K.L. Scipioni, R. Sankar, F. Chou, G. Chang, H. Lin, I. Zeljkovic, V. Madhavan, Nat. Commun. 9 (2018) 1550.